Use of a Movable Nested-Mesh Model for Tracking a Small Vortex

YOSHIO KURIHARA AND MORRIS A. BENDER

Geophysical Fluid Dynamics Laboratory/NOAA, Princeton University, Princeton, NJ 08540

(Manuscript received 7 December 1979, in final form 10 May 1980)

ABSTRACT

The mesh nesting strategy proposed by Kurihara *et al.* (1979) was used to construct a movable, nested-mesh, 11-level primitive equation model. The framework of the model is described in detail.

With the use of a triply nested mesh system with 1°, ⅓° and 1/6° longitude-latitude resolution, a small intense dry vortex in a zonal flow of 10 m s^{-1} was successfully advected for 48 h. The shape of the vortex was well preserved during the time integration which involved over 50 movements of the innermost mesh. The noise, which was excited when a mesh moved, was suppressed in ~4 min after the movement. For comparison, the results from similar experiments performed with reduced inner mesh resolutions are also presented.

1. Introduction

Nested-mesh numerical models are useful operational or research tools for simulating mesoscale meteorological phenomena in the large-scale environment. Nested-mesh models have been developed for the prediction and investigation of tropical cyclones (e.g., Hovermale, 1976; Ookochi, 1978; Ley and Elsberry, 1976; Jones, 1977a) as well as for disturbances in the middle latitudes (e.g., Miyakoda and Rosati, 1977; Shuman, 1978; Sobel and Anthes, personal communication).

As defined by Phillips and Shukla (1973), there are two different strategies, i.e., one-way and two-way nesting, in combining coarse-grid and fine-grid meshes. In the case of a two-way system, two adjacent domains interact with each other all the time. When such a scheme is applied to the time integration of a model with multiple nesting, the predictions on all meshes proceed simultaneously.

To perform the time integration of a two-way system, special caution is required because of the peculiar condition at an interface where two meshes with coarse and fine resolutions meet. In general, numerical characteristics of a solution for the wave equation depend on the grid resolution. This implies that the condition at a mesh interface cannot be compatible with both of the numerical solutions at the two sides of the interface. Thus, a wave is inevitably distorted at a mesh interface. Furthermore, the interface condition may cause the false reflection of waves, generating small-scale noise in the model (Matsuno, 1966). If a movable mesh model is used, noise may also be excited due to dynamical imbalance near the leading and trailing edges of the mesh, just after the movement. The involved numerical problem, therefore, is how to obtain a smoothly connected, noiseless and reasonable solution across the mesh interface during an integration time.

In the present paper, the framework of a movable nested-mesh three-dimensional primitive equation model, which has been constructed at the Geophysical Fluid Dynamics Laboratory/NOAA is described. This model uses the two-way nesting strategy designed by Kurihara *et al.* (1979). In contrast to other two-way nesting methods that have been proposed, the present scheme of nesting has the following features:

1) The dynamical interface, where the two integration domains are dynamically connected to each other, is separated from the mesh interface by a narrow zone of two coarse grid points. Grid data in this region are utilized for the integration of the outer integration domain at each time step. Gridpoints with coarse resolution only are involved in this step of the computation. For the integration of the inner domain, which consists of the abovementioned narrow zone and the enclosed fine-mesh area, flux boundary conditions are computed at the dynamical interface, i.e., on the outer edge of the zone. The distinct advantage of the above strategy is that the mesh interface is free from the immediate impact of the boundary conditions.

In other two-way systems proposed so far, probably without exception, the dynamical interface coincides with the mesh interface. In such a case, boundary conditions at the external boundary points of the fine-mesh area have to be determined by a

scheme which can deal not only with problems resulting from grid resolution changes but also with those concerning dynamical coupling of two integration domains. Grid values or tendencies of certain variables at these points may be derived from coarse-grid data by spatial and temporal interpolation, either linear (Harrison, 1973; Sobel and Anthes, personal communication) or Lagrangian type (Madala and Piacsek, 1975; Jones, 1977a). In the model by Ookochi (1972), an elaborate scheme is used to predict the values at the boundary points. Jones (1977a) states that it was desirable to avoid computing mass convergence across the mesh interface because of its high sensitivity to small errors. He expected some difficulty in the application of the box method (Kurihara and Holloway, 1967) to treat the mesh interface. However, use of the box method did not cause serious problems in the present study. This is perhaps partly due to the separation of the dynamical interface from the mesh interface. Sobel and Anthes (personal communication) also have used the box method to compute mass convergence with apparent success.

2) A large part of the noise excited at a mesh interface usually appears as high-frequency short waves. However, there may be stationary noise generated too. In order to suppress noise, time-damping integration schemes, which yield frequency-selective damping of waves, as well as spatial smoothing schemes have been proposed (e.g., see review by Mesinger and Arakawa, 1976). In the present model, noise is controlled by the application of a time-damping integration method and the occasional use of a spatial smoothing. In the models by Ookochi (1978) and Jones (1977a, 1977b), a spatial smoothing operator is applied at each step in addition to a time-damping scheme. Furthermore, Jones' model employs the upstream method to treat the advection at outflow points of the fine mesh. In some of the experiments with their model, Sobel and Anthes (personal communication) employ a horizontal diffusion term to suppress the noise.

3) The present strategy of mesh nesting in our model allows flexibility in deciding grid resolutions in case of multiple nesting. The ratio of grid increments between the adjacent meshes can be varied easily at each step of nesting. This kind of flexibility virtually does not exist in most of the other models (e.g., Harrison, 1973).

4) The computational method which is used for treating the uniform portions of each grid is also applied to the mesh interfaces in the present study. Consequently, if the above-mentioned grid ratio is made to be unity in the present nested-mesh model, the model simply reduces to a uniform grid model which has no trace of mesh nesting. Whether such a feature is desirable or required is not clear. However, other models do not necessarily possess this property.

In the next section of this paper, the governing equations of the model, the grid system and the two-way nesting strategies are explained. An initialization method for a nested model is the subject of Section 3. Results of the time integration of the triply nested model are presented in Section 4. They are compared in Section 5 with the results from the same models but with coarser inner meshes. Some critical comments on the numerical method used in the present study are made in Section 6. Readers who are not interested in the computational detail of the model but only in the performance of the model should skip Sections 2e–2i and Section 3.

2. Framework of the model

a. Governing equations

A primitive equation model for the dry atmosphere is used in the present study. The governing equations are written as follows in the σ-coordinate system which was originally proposed by Phillips (1957):

EQUATION OF MOTION

$$\frac{\partial}{\partial t}(p_* u) = -D(u) + \left(f + \frac{\tan\phi}{a} u\right) \times p_* v - p_* \frac{\partial \Phi_p}{\alpha \partial \lambda} + {}_H F_\lambda + {}_V F_\lambda, \quad (2.1)$$

$$\frac{\partial}{\partial t}(p_* v) = -D(v) - \left(f + \frac{\tan\phi}{a} u\right) \times p_* u - p_* \frac{\partial \Phi_p}{a \partial \phi} + {}_H F_\phi + {}_V F_\phi, \quad (2.2)$$

where t is the time, λ the longitude, ϕ the latitude, a the radius of the earth, $\alpha = a\cos\phi$, f the Coriolis parameter, u and v the eastward and northward components, respectively, of the horizontal wind and p_* the surface pressure. The operator D denotes the three-dimensional divergence

$$D(\ ) = \frac{\partial(\ )p_* u}{\alpha \partial \lambda} + \frac{\partial(\ )p_* v \cos\phi}{\alpha \partial \phi} + \frac{\partial(\ )p_* \dot{\sigma}}{\partial \sigma}, \quad (2.3)$$

where $\sigma = p/p_*$, p is the pressure, and $\dot{\sigma}$ the vertical σ-velocity defined by $d\sigma/dt$. The pressure gradient force is obtained from the slope of the geopotential Φ_p of an isobaric surface. The last two terms in (2.1) and (2.2) represent the frictional forces due to the horizontal and vertical diffusion of momentum, respectively.

TENDENCY EQUATION

$$\frac{\partial}{\partial t} p_* = -D(1)$$

$$= -\int_0^1 \left(\frac{\partial p_* u}{\alpha \partial \lambda} + \frac{\partial p_* v \cos\phi}{\alpha \partial \phi} \right) d\sigma, \quad (2.4)$$

where the boundary conditions, i.e., $\dot{\sigma} = 0$ at $\sigma = 0$ and 1, are implied.

VERTICAL σ-VELOCITY

$$\dot{\sigma} = \frac{1}{p_*} \left[-\sigma \frac{\partial p_*}{\partial t} - \int_0^\sigma \left(\frac{\partial p_* u}{\alpha \partial \lambda} + \frac{\partial p_* v \cos\phi}{\alpha \partial \phi} \right) d\sigma \right]. \quad (2.5)$$

HYDROSTATIC RELATION

$$\frac{\partial \Phi}{\partial \ln \sigma} = -RT \quad (2.6)$$

or

$$\Phi - RT = \frac{\partial \Phi \sigma}{\partial \sigma}, \quad (2.7)$$

where Φ is the geopotential of a constant σ-surface, T the temperature, and R the gas constant.

THERMODYNAMIC EQUATION

$$\frac{\partial}{\partial t}(p_* T) = -D(T) + \frac{R}{c_p} \frac{T\omega}{\sigma} + {}_H F_T + {}_V F_T, \quad (2.8)$$

where c_p is the specific heat of the air at constant pressure. The vertical p-velocity ω is given by

$$\omega = \frac{dp}{dt} = p_* \sigma \left[\frac{\dot{\sigma}}{\sigma} - \frac{\partial \dot{\sigma}}{\partial \sigma} - \left(\frac{\partial u}{\alpha \partial \lambda} + \frac{\partial v \cos\phi}{\alpha \partial \phi} \right) \right]. \quad (2.9)$$

The last two terms in (2.8) represent the effects of the horizontal and vertical diffusion of heat, respectively.

b. Subgrid-scale mixing.

The subgrid-scale horizontal diffusion is treated by the nonlinear viscosity scheme proposed by Smagorinsky (1963). The general form of the scheme for the σ-coordinate system was formulated by Kurihara and Holloway (1967). In this study, the simplified version explained in the paper by Holloway and Manabe (1971, p. 340) is used. The von Kármán constant, which appears in the viscosity formula, is fixed at 0.2.

The effects of subgrid-scale vertical mixing are represented by the last terms of (2.1), (2.2) and (2.8). These terms may be expressed as

$${}_V F = -g \frac{\partial \tau}{\partial \sigma}, \quad (2.10)$$

$${}_V F_T = -g \frac{\partial H}{\partial \sigma}, \quad (2.11)$$

where τ is the downward diffusive flux of momentum and H the downward diffusive flux of heat. It is assumed that these fluxes vanish at the surface. The fluxes above the surface are estimated by the level 2 formulas of the turbulence closure model derived by Mellor and Yamada (1974). The formulas, which are written in Appendix A, are applicable at any stability condition. The so-called dry adiabatic adjustment scheme is not used in this study.

c. Boundary conditions

The present model is a regional, longitude-latitude grid model. It has a longitudinal span of 35°. A cyclic boundary condition is used at the west and east boundaries.

The model domain is bounded at 2.5 and 39.5°N by open lateral boundaries. It is assumed that the meridional flux, including the diffusive flux, of any meteorological quantity does not contribute to the flux divergence at the boundaries, i.e., $(\partial F \cos\phi)/(\alpha \partial \phi) = 0$, where F is a meridional flux. Thus, the zonal averages of P_*, T, u and v along the boundary are not affected by the advection process and, in particular, the zonal mean of ω vanishes. In addition, it is assumed that the isobaric surface has no curvature at the boundaries, i.e., $(\partial^2 \Phi_p)/(\partial \phi)^2 = 0$.

The boundary condition at the top and the bottom of the model is $\dot{\sigma} = 0$. The vertical diffusive fluxes of momentum and heat do not exist at $\sigma = 0$ as mentioned before, and are set to zero at $\sigma = 1$.

d. Grid system

The horizontal structure of the triply nested mesh system is illustrated in Fig. 1. The resolutions of meshes A, B and C are 1°, ⅓° and 1/6° longitude-latitude, respectively. Each mesh domain is bounded by a mesh interface (solid line in the upper part of Fig. 1). Positioning of the mesh domains B and C are determined with respect to the location of the vortex. The center of mesh C never deviates from the vortex center more than a distance equal to the resolution of mesh B. The center of mesh B is never displaced from the center of mesh C by a distance greater than the resolution of mesh A.

A grid point is placed at the center of each mesh square or box. Meteorological variables are defined at each grid point without horizontal staggering.

In the present model, the entire region is divided into three integration domains. Two neighboring domains are dynamically coupled at the boundary called the dynamical interface, in the course of the

time integration of the model. The dynamical interfaces are indicated by the dashed lines in Fig. 1. These interfaces are separated from the mesh interfaces by a two-grid-point interval. Thus, noise due to dynamical coupling is kept from occurring at the mesh interface where numerical noise tends to take place because of the change of resolution.

The model atmosphere is divided vertically into 11 layers. Each layer has an integer level contained in it and is bounded by half-integer levels. Those levels in the σ coordinate and their approximate heights are shown in Table 1. This vertical division is the same one used by Kurihara and Tuleya (1974) in their hurricane model. The variables u, v, T, ω are defined at the integer levels, whereas Φ and $\dot{\sigma}$ are defined at the half-integer levels.

e. Time integration

A scheme for the numerical integration of a two-way nested-mesh model was examined by Kurihara *et al.* (1979, hereafter referred to as KTB). Their scheme, which will be explained briefly, is used in the present work.

Suppose that a local tendency of a quantity h is determined by

$$\frac{\partial h}{\partial t} = \mathrm{LF} + \mathrm{HF} + \mathrm{DIF}, \tag{2.12}$$

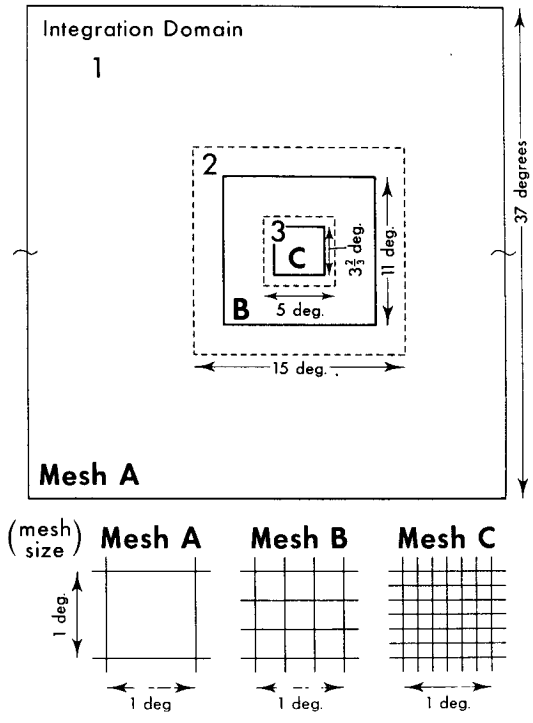

FIG. 1. The horizontal structure of the triply-nested-mesh system, showing the area and grid resolution of the outermost mesh (A), the medium mesh (B) and the innermost mesh (C). Integration domains 1, 2 and 3 are also shown.

TABLE 1. The σ-levels and their approximate heights.

Level k	σ	Height (m)
0.5	0.00000000	
1.0	0.03060333	23637
1.5	0.08318847	17270
2.0	0.12000000	14940
2.5	0.17310091	12616
3.0	0.21500000	11242
3.5	0.26704077	9847
4.0	0.33500000	8328
4.5	0.42025419	6738
5.0	0.50000000	5478
5.5	0.59487807	4168
6.0	0.66500000	3311
6.5	0.74338763	2424
7.0	0.80000000	1843
7.5	0.86092366	1258
8.0	0.89500000	926
8.5	0.93042512	575
9.0	0.95000000	435
9.5	0.96998671	260
10.0	0.97700000	196
10.5	0.98406400	132
11.0	0.99200000	68
11.5	1.00000000	0

where LF denotes the low-frequency tendency due to advection, HF represents the terms contributing to the high-frequency tendency and DIF represents the diffusion terms. The time integration of (2.12) from the time level τ to $\tau + 1$ may be made by the following two-step iterative method (Kurihara and Tripoli, 1976):

$$\left.\begin{aligned}(h^* - h^\tau)/\Delta t &= \mathrm{LF}^\tau + \mathrm{HF}^\tau + \mathrm{DIF}\\ (h^{\tau+1} - h^\tau)/\Delta t &= [(1-\alpha)\mathrm{LF}^\tau + \alpha\mathrm{LF}^*]\\ &\quad + [(1-\beta)\mathrm{HF}^\tau + \beta\mathrm{HF}^*] + \mathrm{DIF}\end{aligned}\right\}, \tag{2.13}$$

where Δt is a time increment and h^* a temporary value. With the use of appropriate weights α and β in (2.13), high-frequency waves can be suppressed while low-frequency waves are preserved. In the present study, α and β are set to 0.506 and 2.5, respectively. Recently, Masuda (1978) pointed out that the use of a large value such as 2 or 3 for β in (2.13) gives rise to a very rapid damping of noise in a primitive equation model.

Eqs. (2.1), (2.2), (2.4) and (2.8) are written in the flux form

$$\frac{\partial}{\partial t}(p_* h) = -D(h) + \cdots.$$

In such a case, the quantity $-D(h) + hD(1)$, which represents the advection of h, should be treated as the LF term of (2.12) and $-hD(1)$ has to be included in the term HF as mentioned in KTB. As to the DIF term, the effect of horizontal diffusion is estimated by an explicit scheme while that of vertical diffu-

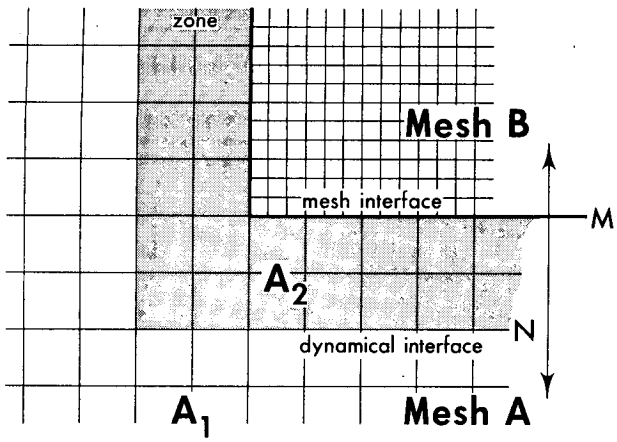

FIG. 2. In a two-dimensional domain, the dynamical interface (line N) is separated from the mesh interface (line M) by a narrow zone A_2 (shaded).

sion is obtained by an implicit method in the present experiment.

The time increments used to integrate the model are 180, 60 and 30 s for the integration domains 1, 2 and 3, respectively. The 180 s integration of the entire three-nest system is complete with the following succession of domain integrations: domain 1, 2, 3, 3, 2, 3, 3, 2, 3, 3. As seen in Fig. 1, the integration domain 2(3) consists of the mesh B(C) area and a narrow zone of coarser resolution, which surrounds the mesh B(C). The ratio of grid size between the narrow zone and the enclosed mesh B is 3:1, while the corresponding ratio for mesh C is 2:1. When the integration for the domain 2(3) is made, the weight β in (2.13) is increased in the narrow zone by the above ratio and takes the value 7.5(5). This was done in order to damp the high-frequency noise in the integration domain uniformly, since the damping rate is inversely proportional to the grid size.

f. Spatial finite differencing

The finite-differencing scheme used to estimate the flux and the gradient of a quantity is described in Section 2d of KTB. In general, the scheme is quite similar to the box method, version 1 (Kurihara and Holloway, 1967). The conservation property for mass, momentum and internal energy is satisfied everywhere. At the mesh interface, the value on the interface is obtained not by the original box method formula but by a different interpolation method (see KTB, Section 2d).

The lateral open-boundary conditions mentioned in Section 2c are implemented at the northernmost and the southernmost boxes of integration domain 1. The flux of any quantity across the northern (southern) boundary of a northernmost (southernmost) box is assumed to be equal to the flux across the southern (northern) interface of the same box. The geopotential of an isobaric surface at the northern (southern) boundary of a northernmost (southernmost) box is obtained by linear extrapolation of geopotentials at the southern (northern) interface and at the grid point of the same box.

g. Dynamical interaction

The dynamical coupling of two adjacent integration domains is performed by applying the strategy of two-way nesting proposed in Section 2c of KTB. The coupling between domains 1 and 2 is now briefly explained as an example. Fig. 2 shows an area which is divided into meshes A and B by the mesh interface M. The dynamical interface N in the figure indicates the boundary between the integration domains 1 and 2. Note that a shaded narrow zone A_2, between the lines M and N, is a part of mesh A and belongs to the integration domain 2. Now suppose that meteorological data are given in A_1, A_2 and B at a certain time level. First, with the use of the data in A_1 and A_2, the prediction with a coarse time step is performed for domain 1, i.e., for the area A_1. During the above prediction, the area A_2 gives a dynamical influence on the area A_1. In the course of numerical integration, the fluxes of various quantities across the interface N as well as the values of certain variables at N are obtained and preserved. These values are used for the dynamical link between domain 2 and domain 1. The prediction for domain 2 is made based on the data in A_2 and B. It proceeds until the time level of domain 2 aligns with that of domain 1. The conditions at the boundary of domain 2 (i.e., at N) are derived successively for each new time level. In KTB, a scheme was proposed which made the sum of the fluxes across N during the integration of domain 2 exactly equal to the flux obtained in the integration for domain 1. This conserving scheme is used in the present study.

h. Mesh movement

The movable meshes B and C are positioned with reference to the location of the disturbance. A reference position is determined in this study from the distribution of the surface pressure in mesh C. Namely, the apparent center of gravity for the following quantity m in the mesh C is taken as the position of the vortex, i.e.,

$$m = \begin{cases} p_0 - p_*, & p_* < p_0 \\ 0, & p_* \geq p_0, \end{cases}$$

where p_0 is a truncation pressure. The quantity p_0 is obtained from

$$p_0 = \gamma(\max p_*) + (1 - \gamma)(\min p_*),$$

where $\max p_*$ and $\min p_*$ are the highest and the lowest value of p_* in mesh C. The weight γ in the

above formula should be chosen so that p_* at a certain distance from the vortex is excluded from the definition of the position of the vortex. In case of an intense vortex, 0.5 is used for γ. When the vortex is weak, a smaller value of γ and/or only a central portion of the mesh C may be used to define the center of gravity for the field m. The above scheme resembles the one used by Jones (1977a).

When the time level of mesh C marches to the same time level as mesh B, the center position of mesh C is checked against the vortex center. If the position difference in any direction exceeds the grid spacing of mesh B, then mesh C is shifted by a multiple, usually one, of the grid distance of mesh B so that the vortex is again found near the center of mesh C. As a result of successive shifts of mesh C, its center may move away from the center of mesh B. If the distance between the two centers becomes larger than the spacing of mesh A, then mesh B is shifted by a multiple of the grid distance of mesh A. Due to the movement of mesh B, mesh C always remains at or near the center of mesh B.

A shift of the nested mesh is achieved by changing coarse-mesh points in front of the leading side of the nest to fine mesh and by reducing the fine-mesh points along the trailing side to coarse mesh. The meteorological values in a new fine-mesh and a new coarse-mesh area can be specified by interpolation and averaging, respectively. The scheme used in this study is the one proposed in Section 3 of KTB, which conserves mass, momentum and internal energy.

i. Noise control

As mentioned in Section 1, a movable nested-mesh model cannot be free from computational noises. In addition to these noises which are due to mesh nesting and mesh movement, noise may also develop in the present model at the northern and the southern lateral sides which are treated as open boundaries. Furthermore, the numerical scheme of the present model uses centered differencing in space which tends to cause a grid-scale irregularity in the predicted fields. All the noises mentioned above must be kept under control during the course of the numerical integration.

The time-integration method mentioned in Section 2e is very effective in damping high-frequency noise. The nonlinear horizontal viscosity works to suppress small-scale quasi-stationary noise. Apparently, as a result of these processes, neither the noise associated with mesh nesting nor with mesh movement caused any computational trouble. It was, nevertheless, found in the preliminary integrations that noise which seemed to be related to the finite-differencing method and noise near the open lateral boundaries could be reduced further with the following additional techniques.

First, in order to suppress the grid-scale irregularity in the mass field, a smoothing operator is applied every 30 time steps for each of the three nests. Namely, the surface pressure and temperature in each box element are replaced by the average of the corresponding variable at the east and the west interface of the box. The smoothing in the meridional direction is carried out in a similar way. (For programming reasons, the meridional smoothing in the present model lags one step behind the zonal smoothing. In the present study, the noise level was found to be smaller when the first three and the last three rows of the mesh A are excluded from the meridional smoothing.) Weakening of the vortex by smoothing is avoided by exempting the central portion (about three-fourths) of mesh C from the smoothing.

A Newtonian-type damping is applied to the flow field within six grid rows from the open lateral boundaries by the addition of the following term to the equation of motion:

$$\frac{\partial \mathbf{v}}{\partial t} = \cdots - (\mathbf{v} - \mathbf{v}_r) t_d^{-1}. \tag{2.14}$$

In (2.14), $\mathbf{v}_r$ is the reference value and t_d the relaxation time. In this study, $\mathbf{v}_r$ is obtained for each grid-point from the average of $\mathbf{v}$ at the latest time level at the four surrounding gridpoints. For the boundary row, the average of only the east and west grid-point values is used to obtain $\mathbf{v}_r$. The tendency due to the above damping term is estimated in an implicit manner. The time t_d is specified by $n\Delta t$, where Δt is the time step for the integration domain 1. The parameter n used for each of the six grid rows is 20, 20, 40, 60, 90 and 120, respectively, increasing from the boundary toward the inner row. An effect similar to the Newtonian damping may be obtained if the eddy diffusion coefficient in the horizontal diffusion terms is increased appropriately.

3. Initial condition

The initial flow field for the present model consists of a cyclonic vortex superposed on a simple zonal flow. The initial mass field is dynamically balanced with the above flow field. The zonal flow has a constant angular velocity which yields an easterly wind of 10 m s^{-1} at 20°N. The cyclonic vortex is nondivergent. Its azimuthal wind speed is a function of radial distance from the vortex center and is given by

$$V = V_m \frac{2R}{R_m}\left[1 + \left(\frac{R}{R_m}\right)^3\right]^{-1} \frac{R_0 - R}{R_0} \tag{3.1}$$

for $R < R_0$ and $V = 0$ for $R \geq R_0$, where R is the radial distance from the center of the vortex. In the present experiment, it is assumed that $V_m = 20$ m s^{-1},

R_m = 100 km and R_0 = 1556 km (equivalent to 14° latitude).

The mass field is obtained from the reverse balance equation in the σ-coordinate system (Sundqvist, 1975), i.e.,

$$\nabla^2\Phi + \frac{\partial}{\alpha\partial\lambda}\left(\frac{RT}{p_*}\frac{\partial p_*}{\alpha\partial\lambda}\right) + \frac{\partial}{\alpha\partial\phi}\left(\cos\phi\frac{RT}{p_*}\frac{\partial p_*}{a\partial\phi}\right) = G, \quad (3.2)$$

where Φ is the geopotential of the σ surface and

$$\nabla^2 = \frac{\partial^2}{\alpha^2\partial\lambda^2} + \frac{\partial}{\alpha\partial\phi}\left(\cos\phi\frac{\partial}{a\partial\phi}\right),$$

$$G = 2J(u,v) + f\zeta - u\beta - \frac{\partial}{\alpha a\partial\phi}[(u^2 + v^2)\sin\phi],$$

$$\zeta = \frac{\partial v}{\alpha\partial\lambda} - \frac{\partial u\cos\phi}{\alpha\partial\phi},$$

$$\beta = \frac{\partial f}{a\partial\phi},$$

$$J = (u,v) = \frac{1}{\alpha a}\left(\frac{\partial u}{\partial\lambda}\frac{\partial v}{\partial\phi} - \frac{\partial u}{\partial\phi}\frac{\partial v}{\partial\lambda}\right).$$

If T and $1/p_*$ in (3.2) are replaced by appropriate constants $T_0(\sigma)$ and $1/p_{*0}$, respectively, then the simplified equations of the Poisson type for p_* and Φ are derived. Namely, the equations for $\sigma = 1$ and $\sigma < 1$ are written, respectively, as follows after some manipulations:

$$\nabla^2 p_* = (p_{*0}/RT_{*0})(G_* - g\nabla^2 z_*), \quad (3.3)$$

$$\nabla^2\Phi = G - (T_0/T_{*0})(G_* - g\nabla^2 z_*), \quad (3.4)$$

where the asterisk denotes the surface value, and $z_* = 0$ in the present study. The right-hand side of the above equations can be calculated from a given wind field. Accordingly, p_* and Φ are obtained by a relaxation method under the appropriate boundary conditions.

In case of a nested-grid system, a special technique may be required to perform the relaxation of the Poisson equation (e.g., Elsberry and Ley, 1976). In the present experiment, the relaxation proceeds inward from the coarsest to the finest grid resolution. In the first stage, the entire model domain is covered by a grid network of mesh A resolution. The forcing, i.e., the right-hand side of (3.3) or (3.4), is computed from the wind data given at each gridpoint. Then, an ordinary relaxation is performed under a proper boundary condition. As noted by Miyakoda and Moyer (1968), the finite-difference form of the Laplacian operator in the balance equation should be consistent with those of the gradient and the divergence operators used in the governing equations. Application of the above rule to the present case, however, causes a checkerboard-type oscillation in the numerical solution of the Poisson equation. Such a noise is associated with the type of centered differencing in space used in the present numerical model. The resulting irregularity is smoothed out by averaging the grid values with the weight ¼, ½, ¼ in each of the longitudinal and the latitudinal directions. The smoothed field defines the mass field in the integration domain 1. It is slightly modified for specifying the mass field in the two-gridpoint zone surrounding mesh B. (Some computational remarks concerning the initialization procedures are given in Appendix B.) In the next stage, proceeding inward, the region consisting of the integration domains 2 and 3 is treated in the same manner as described above except that the grid resolution of mesh B is used. Note that the mass field in the two-gridpoint zone just inside the border of this region is specified in the first stage and serves as the numerical boundary condition in the relaxation process. At the end of the second stage, the mass field in mesh B is determined. In the third stage, the procedures taken in the second stage are repeated for integration domain 3 with the change of grid resolution to that of mesh C. The mass field in mesh C is finally obtained at this stage.

Once the initial field of geopotentials on the constant σ surfaces are obtained, the initial temperature field can be derived easily through the hydrostatic relation.

4. Numerical results

In this section, some numerical results are presented from the movable triply-nested-mesh model described in Section 2. The model was time-integrated starting smoothly from the balanced initial field specified in the preceding section. As mentioned before, the vortex in this experiment is dry and the effect of surface friction is not included, so that any numerical noise, which develops during the integration, can be detected easily.

Fig. 3 shows the distribution of surface pressure at 0, 24 and 48 h in the entire model domain, the medium area (domain 2 and 3) and the innermost domain. The contour lines are drawn by a computer graphic routine and no smoothing is made. The left column of the figure indicates that the nested-mesh system was able to successfully trace the vortex for 48 h. During the integration, mesh C was moved 51 times to the west and three times to the north, and mesh B was shifted west 17 times and north one. The northward movement of the vortex, which is about 68 km for 48 h in the present case, may be associated with the β effect (e.g., Rossby, 1949; Adem, 1956; Madala and Piacsek, 1975).

Despite the movements of the meshes, significant noise is not observable in the surface pressure fields in Fig. 3. The right column of the figure shows a filling tendency of the central surface pressure, from 998.2 to 1002.2 mb, indicating a weakening of the vortex.

The wind fields at level 11 (~68 m level) at 0, 24 and 48 h in each integration domain are presented

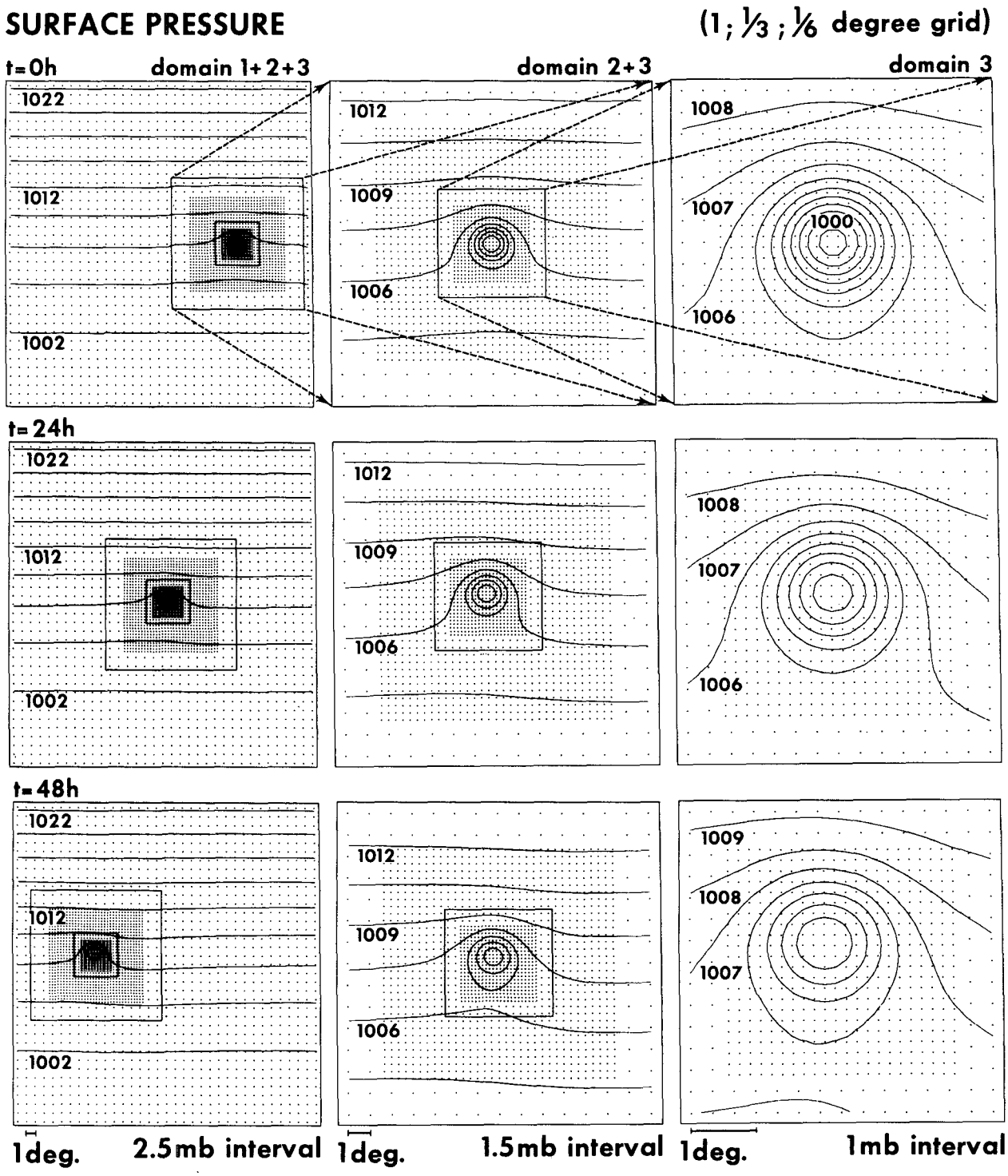

FIG. 3. Distribution of surface pressure at 0, 24 and 48 h for the entire model domain (left column), the medium area (middle column) and the innermost domain (right column). Dots in the figure indicate the gridpoints.

in Fig. 4. The main portion of the vortex is always contained in domain 3 and its shape is preserved well. The maximum wind speed of the vortex changed from 29.9 m s^{-1} at 0 h to 26.5 m s^{-1} at 48 h. This decrease is probably due to the horizontal diffusion of momentum.

Although noise is not noticeable in Figs. 3 and 4, it was excited at the movement of a mesh. However,

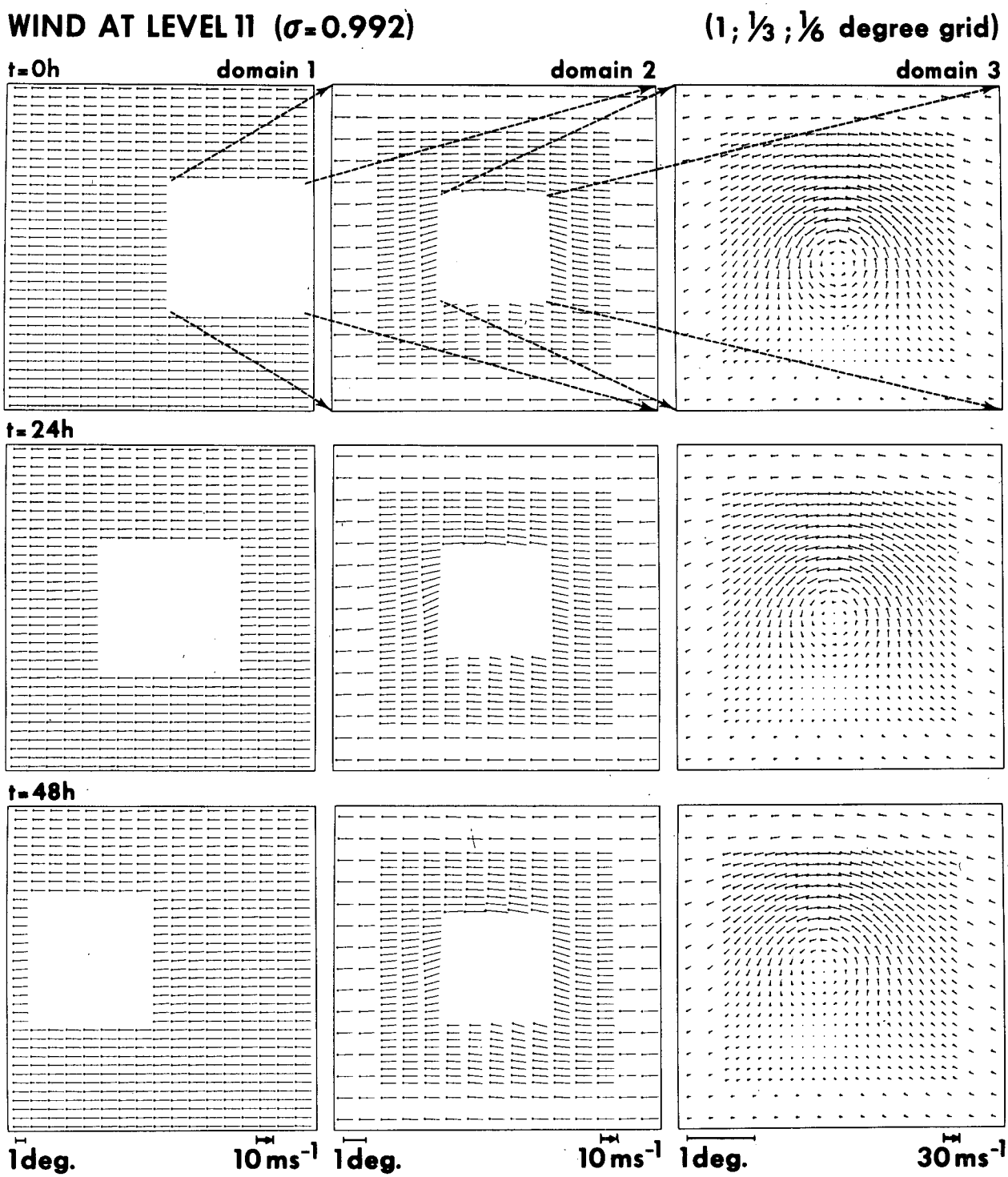

FIG. 4. Wind fields for level 11 at 0, 24, and 48 h, for each of the three integration domains.

as Fig. 5 illustrates, the noise was suppressed very quickly after the movement in the present model. The top portion of the figure shows the fields of surface pressure, the relative vorticity and the vertical p-velocity, respectively, at level 7 (near 800 mb level) in domain 3 at a time 30 s (one time step for mesh C) before the movement of mesh C. The maximum upward velocity is about 5 mm s^{-1}. The middle and the lower parts of the figure show the corresponding fields, respectively, 30 s and 4 min after

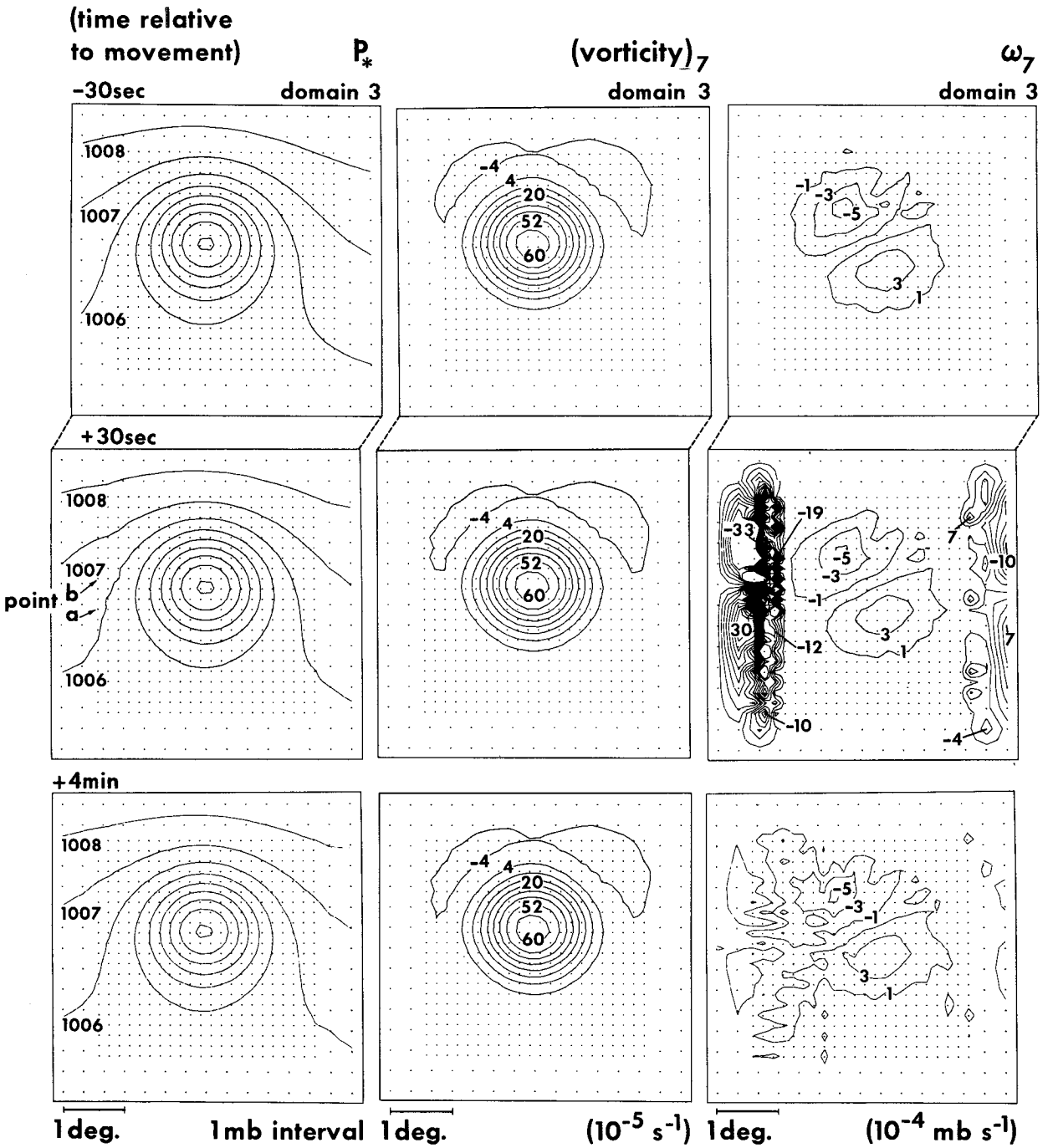

FIG. 5. Distribution of surface pressure, relative vorticity at level 7 and vertical velocity (ω) at level 7, for the innermost domain 30 s before it moved to the west, 30 s after the movement and 4 min after the movement. Two points indicated in the left middle part show the locations for which surface pressure tendency is analyzed in Fig. 6.

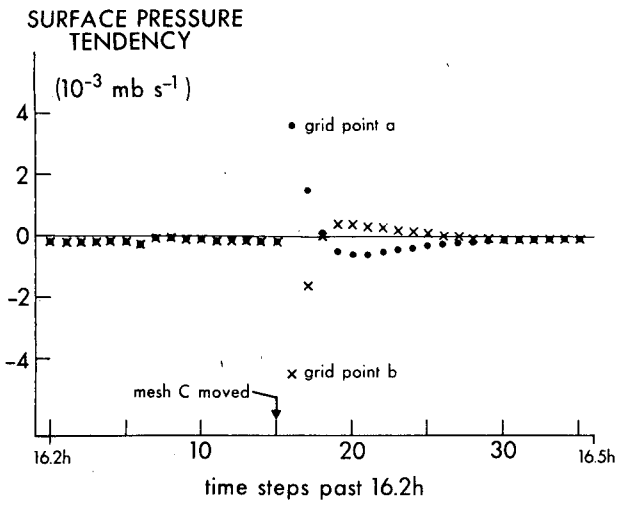

FIG. 6. Surface pressure tendency at gridpoint a (dot) and at gridpoint b (cross mark), plotted every 30 s, during a period just before and after the mesh C moved to the west. Locations of two points are indicated in the left middle part of Fig. 5.

mesh C moved west at 16.325 h. These results are typical of all moves of mesh C. In the surface pressure field, the excited noise is detectable near the leading edge of the mesh at 30 s but it is suppressed in 4 min. In order to show the rate at which the noise was damped, the surface pressure tendencies at two gridpoints are plotted against time in Fig. 6. At these two gridpoints, which are located at the leading edge of mesh C as shown in the left middle portion of Fig. 5, the largest positive and negative tendencies were respectively observed after the mesh movement. In comparison with the corresponding graph by Jones (1977a, Fig. 3), Fig. 6 clearly indicates that damping of the computationally induced noise is significantly faster in the present model. The fields of the wind vector (figures not presented) show no apparent irregularity after the mesh movement. The wind variation from an area where the grid resolution was affected as a result of the mesh movement to an unaffected area also appears quite smooth. Probably, the amplitude of noise in the wind vector field is so small compared to the vector itself that the noise is masked. Small-scale noise in the wind field may manifest itself in the fields of relative vorticity and divergence or the field of vertical motion. According to Jones (1977b) and Sobel and Anthes (personal communication), the vorticity field is very sensitive to nesting noise. In the present experiment, however, the vorticity field remains surprisingly smooth during the integration period even after the mesh movement as shown in the center column of Fig. 5. On the other hand, the mesh movement causes an irregular vertical motion which reached to ~3 cm s^{-1} near the leading edge and ~1 cm s^{-1} near the trailing edge. The right part of Fig. 5 shows that the above noise was suppressed to ~1 mm s^{-1} in only 4 min. It was observed that an abrupt increase of the vertical motion after a mesh movement was always followed by its sharp decline. The efficient control of noise in the present model is largely due to the use of the time-integration scheme described in Section 2e. (The damping rate is reduced when the weight β in the integration scheme is reduced.)

The above analysis results suggest that, at least in the present case, noise was successfully controlled and the impact of mesh nesting on the vortex prediction was probably minimal. However, it should be noted that the experiment in this section was performed with a dry model without the effect of surface friction and, moreover, the treated vortex was almost entirely contained in mesh C. The noise level in case of the general use of the present nesting strategy would be definitely higher than the noise level in this simple case. The proposed scheme has to be examined by applying it to a moist model in which the vortex is not well confined in the finest mesh area. A result for such a case is presented in the last section of this paper.

5. Experiments with coarser resolutions

If the grid resolution is not sufficiently fine relative to the scale of the disturbance being treated, significant numerical dispersion of the disturbance will result due to the scale dependency of the truncation error. It was demonstrated in the preceding section that the shape of the moving vortex was well preserved in the triply nested system with 1°, ⅓° and 1/6° resolution, during the 48 h time integration of the model. In this section, the same vortex is treated with a coarser resolution to determine the effect of the numerical dispersion.

In one experiment, a 48 h integration was performed with the use of a two-nest system. In this case, the latitudinal and longitudinal dimension of the inner mesh was 7° compared to 3⅓° for the innermost mesh of the triply nested system. The grid resolution for the outer and the inner mesh were 1° and ½°, respectively, and the corresponding time increments of 3 min and 1.5 min were used to carry out the time integration. Fig. 7 shows the distributions of the surface pressure, in the entire domain as well as in the inner domain, and the wind at the lowest level in the inner domain at 0, 24 and 48 h. The vortex was successfully advected for 48 h. Its movement was almost the same as that which was obtained in the triply nested model (see Fig. 3). However, the weakening of the vortex was more evident in the double nest system. The maximum wind speed decreased from 29 to 21 m s^{-1} in 48 h. It should be noted here that the above results were obtained for a dry vortex. The degree of sensitivity of vortex intensity to the mesh resolution may be different in the case of a moist vortex.

In the final experiment, the grid resolution of the inner domain for the above double-nested system was increased to 1°. The grid system was thus reduced to a regular, uniform grid of 1° longitude-latitude resolution. The results for the 48 h integration with a 3 min time step are presented in Fig. 8.

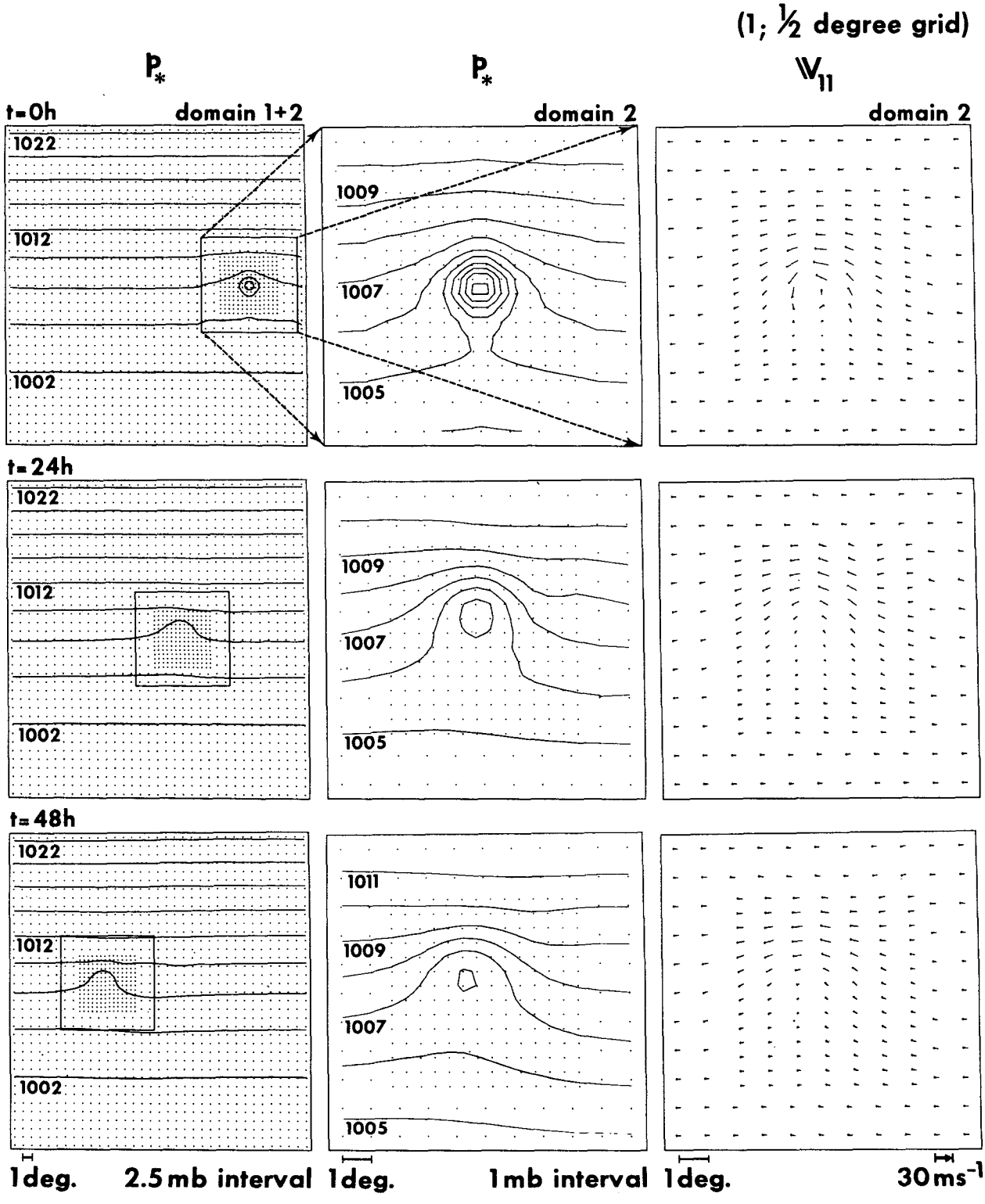

FIG. 7. Results for the double-mesh system with grid resolutions of 1° and 0.5°. Shown here is the distribution of the surface pressure for the entire domain, and the inner domain distribution of surface pressure and level 11 wind, at 0, 24 and 48 h.

The intensity of the vortex was reduced considerably in this experiment. Closed isobars present in the initial surface pressure distribution disappeared by 24 h. The vortex with a circular flow at the initial time and a maximum wind of 27 m s^{-1} deteriorated to a wavy flow pattern with a maximum

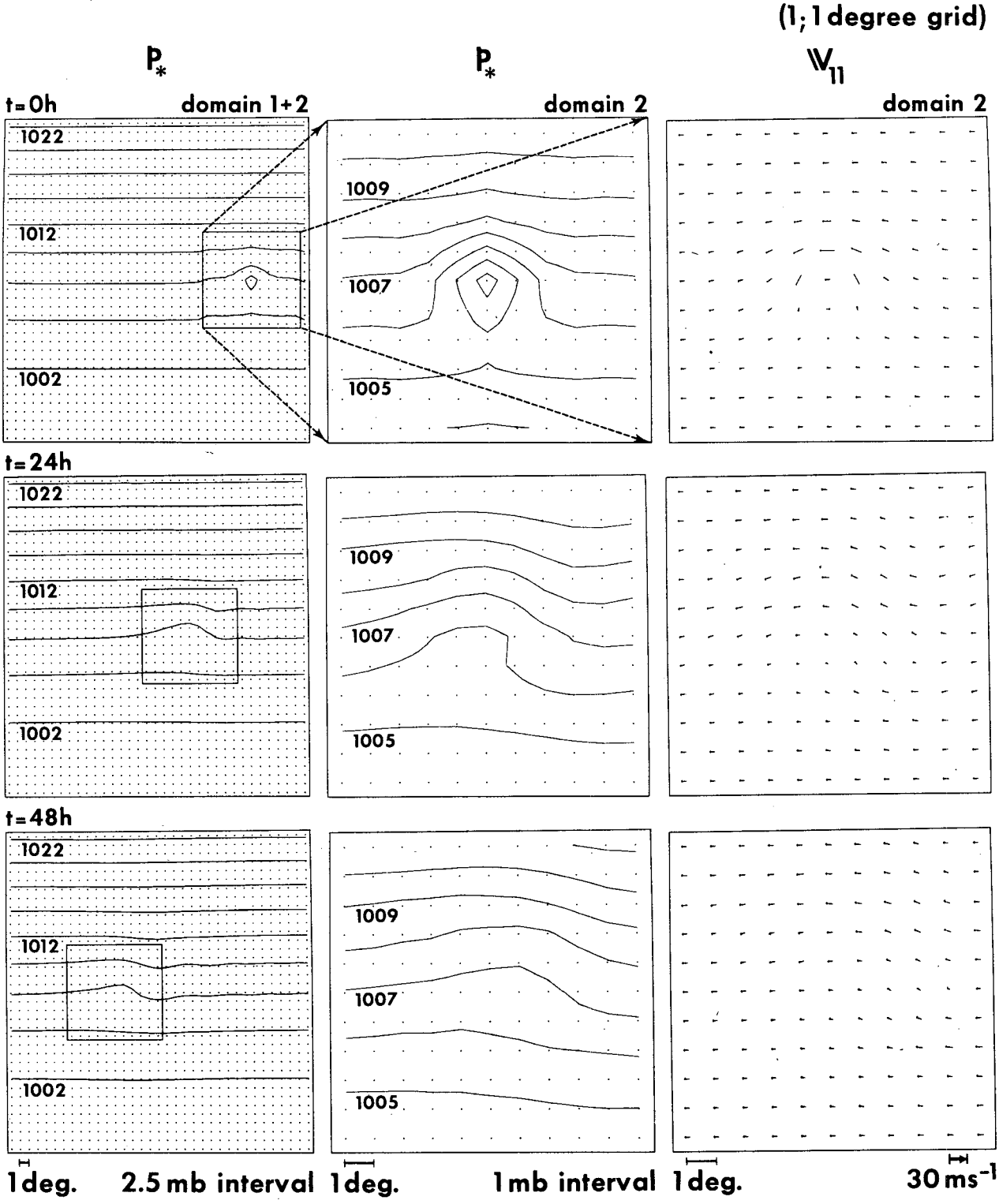

FIG. 8. As in Fig. 7, but with a uniform grid resolution of 1° for both meshes.

of 13 m s^{-1} at 48 h. The disturbance moved primarily westward while causing a trailing noise of small amplitude. The distance that the disturbance moved in 48 h was about 1.5° longitude less than in the experiment with the triply-nested-mesh model.

6. Remarks

The numerical results from the nested mesh model with 1°, ⅓° and 1/6° longitude-latitude resolution demonstrate the capability of this model in tracking an intense small dry vortex. Some features of the adopted strategy of mesh nesting were mentioned in Section 1. Comments on some of the other aspects of the present model are briefly given below.

1) Since the present model has been constructed based on the previously established framework of an earlier hurricane model (Kurihara and Tuleya, 1974), it also used a non-staggered grid system. According to Ookochi (1972), a staggered grid system was most successful in controlling noise in his model. The same system was used by Jones (1977a) and Sobel and Anthes (personal communication). Madala and Piacsek (1975) chose another type of staggered system for their hurricane model. A non-staggered system yields large error in phase speeds of short waves as compared to the staggered systems (e.g., see review by Mesinger and Arakawa, 1976). Although this effect is lessened with the finer resolution attainable in nested-mesh models, it may still cause undesirable features to develop more easily in a non-staggered model unless the short waves with wavelength less than four grid intervals are suppressed adequately. In the present model, damping of these short waves was done through a time-damping integration method and the occasional spatial smoothing.

2) Because of its property of frequency-selective damping, a two-step iteration scheme is used in making the time integration of the present model. It was also used in the models by Ookochi (1972, 1978) and Jones (1977a). In case of the present triply-nested, 11-level primitive equation model, performance of the 48 h integration with 180, 60 and 30 s time steps required 4 h 6 min computer time on the ASC (Advanced Scientific Computer) of Texas Instruments, Inc. Use of a two-step iteration scheme did not necessarily cause a doubling of the computer time, since all diffusion calculations (as well as the convective adjustment for the moist model) are computed only for the first step. However, it still remains one of the important problems in the future to reconsider a time-integration method from the viewpoint of time economy. It should be noted, in this respect, that Madala and Piacsek (1975) used a semi-implicit method in carrying out the time integration of their nested-mesh model.

3) The finite-differencing method applied to the present numerical model has a property to conserve the mass, momentum and internal energy everywhere and preserve the kinetic energy at a place of evenly spaced grids. Since a spatial truncation of a wave varies across the mesh interface, energy conservation may not be required at the interface. It is not quite obvious whether the use of a scheme which conserves first-order quantities such as mass and momentum is desirable or not, since the wave patterns are distorted at the interface. In the present model which uses a mass- and momentum-conserving scheme, smoothness of fields was maintained during 48 h integration. According to the previous study (Kurihara *et al.*, 1979), this scheme will not cause a serious numerical problem if a wave is resolved at the coarse side of the interface. A mass- and momentum-conserving scheme has also been applied to a staggered-grid nested-mesh model (Sobel and Anthes, personal communication). In some other nesting systems, however, it may be necessary to give up the use of a conserving scheme at the interface in order to obtain a smooth field (e.g., Ookochi, 1972; Jones, 1977a). At any rate, the erroneous accumulation of mass or momentum should not occur at the interface of any model.

4) The initialization scheme used in the present study is described in Section 3 and Appendix B. The same static initialization procedure has been successfully employed later in a quadruply nested model of 1°, ⅓°, 1/9° and 1/18° longitude-latitude resolution. In this case, a small circular vortex was assumed at the initial time and a dynamic initialization of the boundary layer (Kurihara and Tuleya, 1978; Kurihara and Bender, 1979) was made after the static initialization. No large noise was excited at the start of the time integration of the model. The proposed scheme has not yet been tested using real wind data including a strong mature tropical cyclone. A test using real data will be made in the near future. In this case, a procedure to decompose the real wind into the rotational and non-rotational components may have to precede the initialization.

5) The numerical model described in Section 2 includes neither moisture nor the effect of surface friction. Although such a simple model is useful in detecting a computationally excited noise, its usefulness as a simulation model is rather limited. Also, the test of numerical schemes with the use of a simple model is not sufficient to infer the general capability of the schemes. Recently, the proposed nesting scheme was applied to a tropical cyclone simulation model which included the effect of surface friction and the hydrologic process. Treatment of these added physical processes in a model is explained in Appendix C. Time integration of the above moist model was performed with a quadruply nested system of 1°, ⅓°, 1/9° and 1/18° longitude-

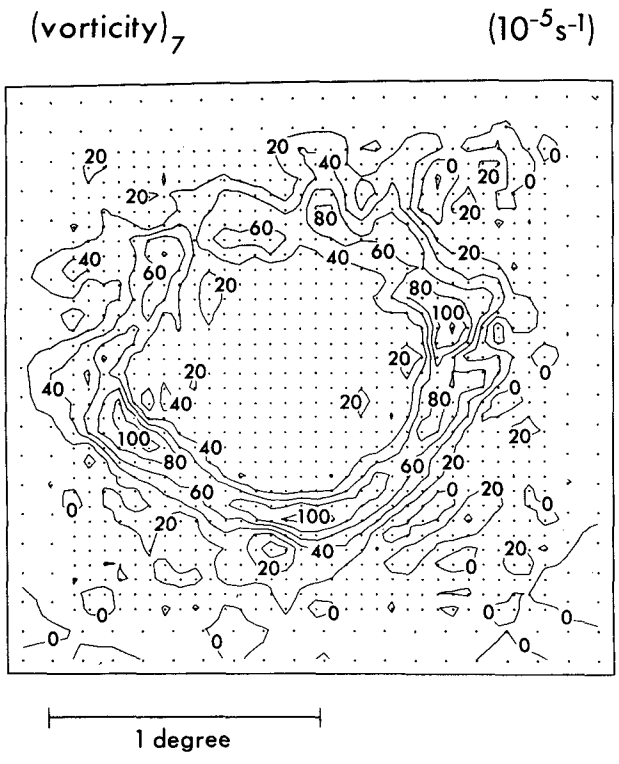

FIG. 9. Distribution of relative vorticity at 15.4 h at level 7 of a moist model, for the innermost domain of a quadruply nested system.

latitude resolutions and 126, 42, 14 and 7 s time steps. In the early period of the integration, the vortex was not well contained in the finest mesh area. This provided a conditon suitable for testing the mesh nesting method. Fig. 9 shows the distribution of relative vorticity at 15.4 h at level 7 of the model (~800 mb level) for the finest mesh and the surrounding area. As mentioned before, the vorticity field is considered very sensitive to nesting noise. The figure indicates that noise is kept under control in the moist model. Time integration was extended to 48 h without any sign of computational difficulty at the mesh interface. The fact that the proposed nesting strategy was successfully applied to a moist model is encouraging.

Acknowledgments. The present authors would like to express their thanks to colleagues at GFDL whose support and assistance helped the progress in the present work. In particular, they appreciate the continuous encouragement by J. Smagorinsky and K. Miyakoda, and many useful advices by R. Tuleya during the course of this study. Also, they are indebted to J. Kennedy for typing the manuscript and to P. Tunison and J. Conner for preparing the figures.

APPENDIX A

Vertical Mixing of Momentum and Heat

The downward fluxes of momentum and heat above the surface layer in the present model are estimated by the level 2 equations of the turbulence closure model derived by Mellor and Yamada (1974). These fluxes are expressed in the σ-coordinate system by

$$(\tau,H) = -g\frac{p_*}{R^2}\frac{\sigma^2}{T^2}\left(K_M\frac{\partial \mathbf{v}}{\partial\sigma}, K_H\frac{\partial\theta}{\partial\sigma}\right), \quad \text{(A1)}$$

where τ is the downward diffusive flux of momentum, $\mathbf{v}$ the horizontal wind, θ the potential temperature and g the acceleration of gravity. The vertical eddy diffusion coefficients are determined by

$$(K_M,K_H) = l^2\left|\frac{\partial \mathbf{v}}{\partial z}\right|(S_M,S_H), \quad \text{(A2)}$$

where l is the mixing length and S_M and S_H are the stability-dependent factors. In the present study, Blackadar's formula (1962) is used to specify l, i.e.,

$$l = \frac{kz}{1 + kz/l_0}, \quad \text{(A3)}$$

with $k = 0.4$ and $l_0 = 30$ m. To obtain the stability factors, the Richardson number Ri and the flux Richardson number Rf are computed first:

$$\mathrm{Ri} = \frac{g}{T}\left(\frac{\partial T}{\partial z} + \frac{g}{c_p}\right)\left|\frac{\partial \mathbf{v}}{\partial z}\right|^{-2}, \quad \text{(A4)}$$

$$\mathrm{Rf} = 0.725[\mathrm{Ri} + 0.186 - (\mathrm{Ri}^2 - 0.316\,\mathrm{Ri} + 0.0346)^{1/2}]. \quad \text{(A5)}$$

The following formulas give S_M and S_H:

$$S_M = \begin{cases} 0 & \text{for Rf} > 0.213 \\ (1 - \mathrm{Rf})^{1/2}\left[\dfrac{5.771(0.229 - 0.845\gamma)(0.173 - 0.470\gamma)}{(0.229 - 0.689\gamma)}\right]^{3/2} & \text{for Rf} \leq 0.213, \end{cases} \quad \text{(A6)}$$

where

$$\gamma = \mathrm{Rf}(1 - \mathrm{Rf})^{-1},$$
$$S_H = S_M \,\mathrm{Rf}\,\mathrm{Ri}^{-1} \tag{A7}$$

APPENDIX B

Remarks on the Numerical Scheme of Relaxation

The simplified reverse balance equation, i.e., Eqs. (3.3) and (3.4) in the text, in the case of a flat surface condition, are written

$$\nabla^2 p_* = (p_{*0}/RT_{*0})G_*, \tag{B1}$$
$$\nabla^2 \Phi = G - (T_0/T_{*0})G_*. \tag{B2}$$

In order to solve the above Poisson-type equations, it is assumed in the present study that p_* and Φ are cyclic at the west and the east ends of the channel domain. The conditions at the south and the north boundaries are derived from the assumption of the geostrophic balance in the background zonal fields. Denoting a zonal field by an overbar, the geostrophic relation in the σ-coordinate system becomes

$$\frac{\partial \ln \bar{p}_*}{a\partial\phi} = -\frac{1}{R\bar{T}_*}\left(f + \frac{\tan\phi}{a}\bar{u}_*\right)\bar{u}_* \tag{B3}$$

$$\frac{\partial \bar{\Phi}}{a\partial\phi} = -\left(f + \frac{\tan\phi}{a}\bar{u}\right)\bar{u} - R\bar{T}\frac{\partial \ln \bar{p}_*}{a\partial\phi}$$
$$= -f\left(\bar{u} - \frac{\bar{T}}{\bar{T}_*}\bar{u}_*\right) - \frac{\tan\phi}{a}\left(\bar{u}^2 - \frac{\bar{T}}{\bar{T}_*}\bar{u}_*{}^2\right). \tag{B4}$$

Assigning appropriate values $\bar{p}_{*0}$ and $\bar{T}_0(\sigma)$, respectively, to $\bar{p}_*$ and $\bar{T}(\sigma)$ at a certain latitude ϕ_0, and approximating $\bar{T}_*$ in (B.3) with $\bar{T}_{*0}$, $\bar{T}/\bar{T}_*$ in (B4) with $\bar{T}_0/\bar{T}_{*0}$, $\bar{p}_*$ and Φ can be solved from the above equations once $\bar{u}$ is given. [Note that $\bar{\Phi}$ at ϕ_0 is related to $\bar{T}_0(\sigma)$ through the hydrostatic relation.] The lateral boundary values of $\bar{p}_*$ and $\bar{\Phi}$ at each of the two grid rows nearest to the boundaries are obtained and fixed during the numerical process of the relaxation.

The finite-difference Laplacian operator in the present model is derived as follows. Using the differencing scheme described in Section 2d of KTB, the gradient of a quantity ψ at a box i,j is given by

$$\left(\frac{\partial\psi}{\alpha\partial\lambda}\right)_{i,j} \to \{[a_{i,j}\psi_{i+1,j} + (1 - a_{i,j})\psi_{i,j}] - \psi_{i,j}\}E_{i,j} + \{\psi_{i,j} - [(1 - b_{i,j})\psi_{i,j} + b_{i,j}\psi_{i-1,j}]\}W_{i,j}, \tag{B5}$$

$$\left(\frac{\partial\psi}{a\partial\phi}\right)_{i,j} \to \{[c_{i,j}\psi_{i,j+1} + (1 - c_{i,j})\psi_{i,j}] - \psi_{i,j}\}N_{i,j} + \{\psi_{i,j} - [(1 - d_{i,j})\psi_{i,j} + d_{i,j}\psi_{i,j-1}]\}S_{i,j}, \tag{B6}$$

where E, W, N and S are the weights, i.e., the length of the east, west, north and south interface of the box divided by its area, and the coefficients are dependent on the dimensions of boxes, i.e.,

$$a_{i,j} = \Delta\lambda_{i,j}/(\Delta\lambda_{i+1,j} + \Delta\lambda_{i,j}),$$
$$b_{i,j} = \Delta\lambda_{i,j}/(\Delta\lambda_{i,j} + \Delta\lambda_{i-1,j}),$$
$$c_{i,j} = \Delta\phi_{i,j}/(\Delta\phi_{i,j+1} + \Delta\phi_{i,j}),$$
$$d_{i,j} = \Delta\phi_{i,j}/(\Delta\phi_{i,j} + \Delta\phi_{i,j-1}).$$

The right-hand side of (B5) and (B6) may be expressed as $(\nabla_\lambda\psi)_{i,j}$ and $(\nabla_\phi\psi)_{i,j}$, respectively. The finite-difference divergence of $\nabla\psi$, the components of which are $\nabla_\lambda\psi$ and $\nabla_\phi\psi$, yields the finite-difference expression for the Laplacian of ψ:

$$(\nabla^2\psi)_{i,j} \to [a_{i,j}(\nabla_\lambda\psi)_{i+1,j} + (1 - a_{i,j})(\nabla_\lambda\psi)_{i,j}]E_{i,j} - [(1 - b_{i,j})(\nabla_\lambda\psi)_{i,j} + b_{i,j}(\nabla_\lambda\psi)_{i-1,j}]W_{i,j} + [c_{i,j}(\nabla_\phi\psi)_{i,j+1} + (1 - c_{i,j})(\nabla_\phi\psi)_{i,j}]N_{i,j} - [(1 - d_{i,j})(\nabla_\phi\psi)_{i,j} + d_{i,j}(\nabla_\phi\psi)_{i,j-1}]S_{i,j}. \tag{B7}$$

using (B5) and (B6), Eq. (B7) can be rearranged to the following nine-point formula:

$$(\nabla^2\psi)_{i,j} \to g_1\psi_{i+2,j} + g_2\psi_{i,j+2} + g_3\psi_{i-2,j} + g_4\psi_{i,j-2} + g_5\psi_{i+1,j} + g_6\psi_{i,j+1} + g_7\psi_{i-1,j} + g_8\psi_{i,j-1} + g_0\psi_{i,j}, \tag{B8}$$

where g_n ($n = 0, 1, \ldots, 8$) represents the coefficient to be specified for the grid point i,j.

As mentioned in Section 3, the solution ψ_u, of the relaxation obtained with (B8), tends to exhibit a computational mode, i.e., a grid-scale irregularity. A smooth field ψ_s is obtained by taking a spatial average of ψ_u. In the nested mesh model, the grid-point values thus obtained define the field outside the two-gridpoint frame surrounding the inner mesh. The effect of smoothing on the physical mode must be removed from the smoothed field within the frame, since those points in the frame provide the numerical boundary condition in making the relaxation for the inner area enclosed by the frame. Within the western and the eastern frame, this is done by adding $(\Delta\psi)_j$ to $(\psi_s)_{ij}$, where

$$(\Delta\psi)_j = \tfrac{1}{4}(\bar{\psi}_u^{j+1} + 2\bar{\psi}_u^{j} + \bar{\psi}_u^{j-1}) - \bar{\psi}_s^{j},$$

where the overbar with index j means the two-point average on the jth row within the frame. Correction for ψ_s in the northern and the southern frames is made similarly. A correction amount for the four

points at each of the four frame corners is given by the difference between the four-point averages of ψ_u and ψ_s. The above corrections may cause a small but abrupt change in the ψ-field across the outer edge of the frame. Despite such a discontinuity, which can be damped quickly after the start of time integration of the model, the correction is needed in order to obtain an accurate solution for the inner mesh region. Since the relaxation for the inner area is treated with a fine resolution, new values in the east and the west frames at the same latitude as each inner area grid row are obtained by linear interpolation in the meridional direction, using only the coarse points in the frame. For the grid columns, new values in the north and the south frames at the same longitude as each inner area grid column are obtained similarly using the data from the coarse gridpoints in the frame.

APPENDIX C

A Model with Hydrologic Cycle

The hydrologic cycle in a moist model is expressed by the equation for the mixing ratio of water vapor, i.e.,

$$\frac{\partial}{\partial t}(p_* r) = -D(r) + {}_H F_r + {}_V F_r + \mathrm{RCON}, \quad \text{(C1)}$$

where r is the mixing ratio of the water vapor, and the last three terms represent the effects of horizontal diffusion, of vertical diffusion, and of the condensation and convection process, respectively. Also a term corresponding to RCON has to be added to the thermodynamic equation (2.8).

In the models currently in use by the hurricane project at GFDL, the air-sea interaction process is estimated in the Monin-Obukhov framework as described by Kurihara and Tuleya (1974, p. 897). The effects of horizontal and vertical diffusion are evaluated by the schemes mentioned in Section 2b and Appendix A. [In a moist model, Eq. (A4) is modified by adding 0.61 $T\ \partial r/\partial z$ to $\partial T/\partial z$.] The dry convective adjustment is not used.

The effect of free moist convection is incorporated in the model through a method of moist convective adjustment. The adjustment scheme used is the same one outlined by Kurihara and Tuleya (1974, pp. 898–900) with two changes. The parameter D_0 appearing in (3.34) in their paper is modified so that it is 500 m above the 700 m height, 0 m at sea level, and linearly increases in the layer between the 0 and 700 m levels. Also, the following change is made in adjustment speed. If cumulus convection develops in the model for a given initial condition, then the large-scale thermodynamical state is altered to a new stable state through the adjustment, at the first step in the time integration of the model. After the first step, however, the adjustments of T and r are moderated by multiplying a factor $\Delta t/t_0$, where Δt is the marching step and t_0 the relaxation time, which serves to spread the adjustment over a longer period. By the use of the relaxation time, which is assumed to be 5 min, the adjustment is made smoothly across the mesh interfaces both timewise and spacewise.

In Section 2i, noise control in the nested-mesh model is discussed. In case of the moist model, Newtonian damping in the form of (2.14) is applied to u, v and p_* within six grid rows from the open lateral boundaries of mesh A. It is also applied to r, if r is greater than the reference value. The reference values of u, p_* and r at the first row from the northern and southern boundaries are computed from the averages of the east and the west points, while the reference value for v includes the value at the inner (south or north) gridpoint which is weighted double in taking the average. The reference value for gridpoints on the second through sixth row from the boundary is simply the average of values at the four surrounding gridpoints for all variables. Also, as mentioned in Section 2i, the fields of p_* and T are smoothed every 30 steps for each mesh. The 1:2:1 smoothing in both the west–east and north–south directions is applied, except that west–east smoothing only is made for the first row from the northern and southern boundaries of mesh A.

An alternate scheme to control noise is to eliminate Newtonian dumping for u and v and increase the value of the von Karman constant used in the formula for horizontal viscosity, at the border area in mesh A. Specifically, the square of the constant at the fifth through the first grid rows from the boundary may be set to 0.2, 0.4, 0.6, 0.8 and 1.0, compared to 0.04 for all other points. In this case, Newtonian damping is needed only for r, or for r and p_*.

REFERENCES

Adem, J., 1956: A series solution for the barotropic vorticity equation and its application in the study of atmospheric vortices. *Tellus*, **8**, 364–372.

Blackadar, A. K., 1962: The vertical distribution of wind and turbulent exchange in neutral atmosphere. *J. Geophy. Res.*, **67**, 3095–3102.

Elsberry, R. L., and G. W. Ley, 1976: On the strategy of initializing nested grid meshes in numerical weather prediction. *Mon. Wea. Rev.*, **104**, 797–799.

Harrison, E. J., 1973: Three-dimensional numerical simulations of tropical systems utilizing nested finite grids. *J. Atmos. Sci.*, **30**, 1528–1543.

Holloway, J. L., Jr., and S. Manabe, 1971: Simulation of climate by a global general circulation model. *Mon. Wea. Rev.*, **99**, 335–370.

Hovermale, J. B., 1976: The movable fine mesh (MFM)—a new operational forecast model. Tech. Proc. Bull. No. 160, Tech. Serv. Br., Meteor. Serv. Div., Nat. Wea. Serv., 5 pp.

Jones, R. W., 1977a: A nested grid for a three-dimensional model of a tropical cyclone. *J. Atmos. Sci.*, **34,** 1528–1553.

——, 1977b: Noise control for a nested grid tropical cyclone model. *Contrib. Atmos. Phys.*, **50,** 393–402.

Kurihara, Y., and M. A. Bender, 1979: Supplementary note on "A scheme of dynamic initialization of the boundary layer in the primitive equation model". *Mon. Wea. Rev.*, **107,** 1219–1221.

——, and J. L. Holloway, Jr., 1967: Numerical integration of a nine-level global primitive equations model formulated by the box method. *Mon. Wea. Rev.*, **95,** 509–530.

——, and G. J. Tripoli, 1976: An iterative time integration scheme designed to preserve a low-frequency wave. *Mon. Wea. Rev.*, **104,** 761–764.

——, ——, and M. A. Bender, 1979: Design of a movable nested-mesh primitive equation model. *Mon. Wea. Rev.*, **107,** 239–249.

——, and R. E. Tuleya, 1974: Structure of a tropical cyclone developed in a three-dimensional numerical simulation model. *J. Atmos. Sci.*, **31,** 893–919.

——, ——, 1978: A scheme of dynamic initialization of the boundary layer in a primitive equation model. *Mon. Wea. Rev.*, **106,** 114–123.

Ley, G. W., and R. L. Elsberry, 1976: Forecasts of Typhoon Irma using a nested-grid model. *Mon. Wea. Rev.*, **104,** 1154–1161.

Madala, R. V., and S. A. Piacsek, 1975: Numerical simulation of asymmetric hurricane on a β-plane with vertical shear. *Tellus*, **27,** 453–468.

Masuda, Y., 1978: A time integration scheme to damp efficiently high-frequency noises. *J. Meteor. Soc. Japan*, **56,** 571–583.

Matsuno, T., 1966: False reflection of waves at the boundary due to the use of finite differences. *J. Meteor. Soc. Japan*, **44,** 145–157.

Mellor, G. L., and T. Yamada, 1974: A hierarchy of turbulence closure models for planetary boundary layers. *J. Atmos. Sci.*, **31,** 1791–1806.

Mesinger, F., and A. Arakawa, 1976: Numerical methods used in atmospheric models, Vol. 1. GARP Publ. Ser. No. 17, Joint Organizing Committee GARP, 64 pp.

Miyakoda, K., and R. W. Moyer, 1968: Method of initialization for dynamical weather forecasting. *Tellus*, **20,** 115–128.

——, and A. Rosati, 1977: One-way nested grid models: The interface conditions and the numerical accuracy. *Mon. Wea. Rev.*, **105,** 1092–1107.

Ookochi, Y., 1972: A computational scheme for the nesting fine mesh in the primitive equation model. *J. Meteor. Soc. Japan*, **50,** 37–48.

——, 1978: Preliminary test of typhoon forecast with a moving multi-nested grid (MNG). *J. Meteor. Soc. Japan*, **56,** 571–583.

Phillips, N. A., 1957: A coordinate system having some special advantages for numerical forecasting. *J. Meteor.*, **14,** 184–185.

——, and J. Shukla, 1973: On the strategy of combining coarse and fine grid meshes in numerical weather prediction. *J. Appl. Meteor.*, **12,** 763–770.

Rossby, C.-G., 1949: On a mechanism for the release of potential energy in the atmosphere. *J. Meteor.*, **6,** 163–180.

Shuman, F. G., 1978: Numerical weather prediction. *Bull. Amer. Meteor. Soc.*, **59,** 5–17.

Smagorinsky, J., 1963: General circulation experiments with the primitive equations: I. The basic experiment. *Mon. Wea. Rev.*, **91,** 99–164.

Sundqvist, H., 1975: Initialization for models using sigma as the vertical coordinate. *J. Appl. Meteor.*, **14,** 153–158.